



Continuous daytime and nighttime forecast of atmospheric optical turbulence from numerical weather prediction models

FLORIAN QUATRESOOZ,^{1,3} RYAN GRIFFITHS,^{2,*}  LISA BARDOU,²
RICHARD WILSON,² JAMES OSBORN,²  DANIELLE
VANHOENACKER-JANVIER,¹ AND CLAUDE OESTGES¹

¹*ICTEAM Institute, Université Catholique de Louvain (UCLouvain), Louvain-la-Neuve, Belgium*

²*Centre for Advanced Instrumentation, Durham University, Durham, United Kingdom*

³*florian.quatresooz@uclouvain.be*

^{*}*ryan.griffiths@durham.ac.uk*

Abstract: Future satellite-to-ground optical communication systems will benefit from accurate forecasts of atmospheric optical turbulence; namely for site selection, for the routing and the operation of optical links, and for the design of optical communication terminals. This work presents a numerical approach based on the Weather Research and Forecasting software that enables continuous forecast of the refractive index structure parameter, C_n^2 , vertical profiles. Two different C_n^2 models are presented and compared. One is based on monitoring the turbulent kinetic energy, while the other is a hybrid model using the Tatarskii equation to depict the free atmosphere region, and the Monin-Obukhov similarity theory for describing the boundary layer. The validity of both models is assessed by using thermosonde measurements from the Terrain-induced Rotor Experiment campaign, and from day and night measurements of the coherence length collected during a six-day campaign at Paranal observatory by a Shack-Hartmann Image Motion Monitor. The novelty of this work is the ability of the presented approach to continuously predict optical turbulence both during daytime and nighttime, and its validation with measurements in day and night conditions.

Published by Optica Publishing Group under the terms of the [Creative Commons Attribution 4.0 License](https://creativecommons.org/licenses/by/4.0/). Further distribution of this work must maintain attribution to the author(s) and the published article's title, journal citation, and DOI.

1. Introduction

Atmospheric turbulence leads to fluctuations of the atmospheric refractive index, modifying the trajectory of optical waves. This phenomenon is often referred to as optical turbulence (OT), and has been extensively studied at astronomical sites. Indeed, it is a major concern for ground-based optical astronomy, that motivated the development of adaptive optics to correct the aberrations induced by the atmosphere in real-time [1].

Nowadays, the characterization of OT is also of interest for free-space optical communications (FSOC), especially for future optical communication systems between satellites and the ground. For such systems, OT leads to wavefront distortions, intensity fluctuations, and signal fading [2]. It is therefore important to consider its impact on the design of optical communication systems (e.g., in the link budgets), on the selection of optical ground station (OGS) locations, and on the networking and scheduling of communication links [3].

Different metrics have been defined to characterize OT, such as the vertical profile of the refractive index structure parameter C_n^2 . This is a statistical quantity describing how strong the atmospheric refractive index fluctuations are. Other metrics involve the scintillation index, the seeing, the coherence length (also named Fried parameter), the isoplanatic angle, etc., that are integrated quantities of the C_n^2 profiles. [2,4] Moreover, two complementary approaches for

characterizing OT have been developed: monitoring with scientific instruments, and modelling based on theoretical insights.

Until recently, the monitoring of OT has been mostly conducted at astronomical sites. It relies on dedicated instruments, recording integrated parameters (e.g., seeing using a Differential Image Motion Monitor - DIMM [5–7]), or measuring vertical profiles of C_n^2 (for example, using Scintillation Detection and Ranging - SCIDAR [8,9], or Slope Detection and Ranging - SLODAR [10,11]). C_n^2 profiling instruments currently used are relatively large and expensive, motivating the development of smaller instruments, such as Shack-Hartmann Image Motion Monitor [12] (SHIMM), or Ring-Image Next Generation Turbulence Sensor [13] (RINGSS). Those instruments are of great interest to evaluate the quality of future OGS sites, and measurement campaigns are currently in progress [14].

Regarding the modelling of OT, it is usually conducted with models of C_n^2 derived from empirical measurements, or from theoretical approaches based on Kolmogorov theory of turbulence [15]. Of particular interest are models including the geographic and temporal variations of C_n^2 derived from local meteorological quantities. The latter may be obtained from numerical weather prediction (NWP) simulations for example, enabling the forecasting of OT.

The forecast of OT for optical communication sites is the focus of this work. It has previously been studied at astronomical sites, namely to assist the scheduling of observations, and to conduct site selection [16]. Several approaches are available in the literature, and can be classified based on the C_n^2 model they rely on: theoretical models using the Tatarskii's equations [16–18], empirical models (such as the Trinquet-Vernin model [19,20]), or numerical models solving for the turbulent kinetic energy (TKE). The Astro-Meso-Nh [21,22] model belongs to this last category, and numerical models integrated with the Weather Research and Forecasting (WRF) software have also been presented [23–25].

Nevertheless, most models presented above consider astronomical sites in nighttime conditions. Their validity for optical communication sites, and daytime conditions, must therefore be assessed, as conducted in this work. The forecast of OT for optical communications is challenging, namely because daytime turbulence is increased in the boundary layer and due to the lack of daytime OT measurements. An accurate description of this layer is one motivation to rely on models solving for the TKE. Alternatively, hybrid C_n^2 models have been suggested, and consider the boundary layer and the free atmosphere differently [26,27]. The ground C_n^2 value may be obtained empirically [28,29], or with Monin-Obukhov similarity theory [30,31].

Based on those observations, this paper presents two different C_n^2 models that can be used to conduct nighttime and daytime predictions of C_n^2 profiles. Both models use NWP simulation outputs (from WRF software) for forecasting OT, and are applied at a non-astronomical site (Three Rivers, CA, USA), and at an astronomical site (Paranal observatory, Chile). One of the models relies on the TKE [32], while the other is a hybrid model using Tatarskii's equation and Monin-Obukhov similarity theory [33]. The validation of the free atmosphere profiling capabilities of those models is conducted thanks to a comparison with thermosonde measurements from the Terrain-induced Rotor Experiment (T-REX) campaign. The validation of their boundary layer predictions is achieved using continuous Fried parameter measurements at Paranal. Daytime and nighttime validations are conducted, highlighting the model performance in different conditions. Some insights about the number of vertical levels to consider in the NWP simulations are also presented, and a study of the daytime exponent influencing the decrease of C_n^2 in the boundary layer with the altitude is conducted.

Section 2 details the general approach used to forecast OT using NWP simulations, and presents the chosen parameterization. Then, Section 3 describes the two C_n^2 models considered, while Section 4 provides the validation of the approach with thermosonde measurements (Section 4.1), and Fried parameter measurements (Section 4.2).

2. Parameterization of numerical weather prediction simulations

2.1. General approach

Inspired from the literature associated to OT forecasting for astronomical applications [16,24,34,35], Figure 1 depicts the approach used to obtain C_n^2 profiles above a location of interest. It involves two main steps: the NWP simulations, and the application of a C_n^2 model.

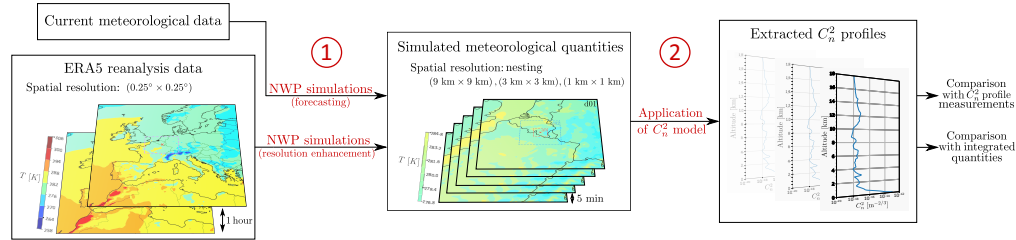


Fig. 1. General approach to conduct OT forecast from NWP simulations. The two main steps are highlighted: the NWP simulations (1) and the application of C_n^2 models (2). Figure adapted from [32].

2.1.1. NWP simulations

The first step presented in Figure 1 uses meteorological data as inputs, and forecasts their evolution over a three-dimensional (3D) domain thanks to the NWP software. The objectives of this step are twofold: (i) using current meteorological data to forecast their evolution in the following hours or days, (ii) improving the spatial and temporal resolutions of the available meteorological data. As an output, a 3D grid of meteorological quantities (e.g., temperature, pressure, wind speed, etc.) at the desired location is obtained, with its time-evolution monitored.

In this work, initial meteorological data come from the ERA5 reanalysis database from ECMWF [36]. They offer a horizontal resolution of $(0.25^\circ \times 0.25^\circ)$, with 37 vertical levels. Their temporal resolution is one hour. The NWP software used is the WRF software, version 4.2, developed conjointly by the National Center for Atmospheric Research (NCAR), the National Oceanic and Atmospheric Administration (NOAA), the Air Force Weather Agency (AFWA), the Naval Research Laboratory (NRL), the University of Oklahoma, and the Federal Aviation Administration (FAA) [37]. Its parameterization is described in Section 2.2 and enables retrieval of meteorological data having a horizontal resolution of one kilometer, with a temporal resolution of 5 minutes, as depicted in the center of Figure 1.

2.1.2. Application of C_n^2 models

The second step starts from the high-resolution forecast meteorological data and applies a parametric C_n^2 model such that C_n^2 profiles above the location of interest can be extracted. The temporal evolution of those profiles is also monitored. They are then compared with measurements in order to validate the models, and used to compute important OT quantities, such as the seeing or the scintillation index, that are related to C_n^2 profiles with analytical expressions. The C_n^2 models chosen in this work are presented in Section 3.

2.2. Weather research and forecasting software

The WRF software is a mesoscale model that can simulate atmospheric phenomena ranging from kilometers to hundreds of kilometers above a limited area of Earth. It relies on grid nesting, that is, the imbrication of several domains having different horizontal resolutions, in order to increase the resolution over the region of interest. It is used for various research applications

and has previously been used for OT forecast at astronomical sites [20,24,25] and for optical communications [38].

2.2.1. Spatial resolution and nested domains

The configuration of WRF grid parameters is presented in Table 1. One-way nesting with 3 domains is implemented, starting with an initial grid size of 9 km, and ending with a grid size of 1 km in the inner domain (horizontal resolution). Vertically, 100 pressure levels ranging from the ground to 5000 Pa (approximately 20 km of altitude) are chosen, and are non-equally distributed: close to the ground, the spacing between levels is smaller (~50 m), while it is coarser at high altitudes (~250 m). This is illustrated in Figure 2, showing the WRF configurations used for the TREX thermosonde study conducted in Section 4.1, and at Cerro Paranal in Section 4.2. The different domains, centred on the location of interest, are clearly noticeable on the left part of the figure. The topography of the inner domain is depicted in the middle, while the right part of the figure gives the distribution of the pressure levels.

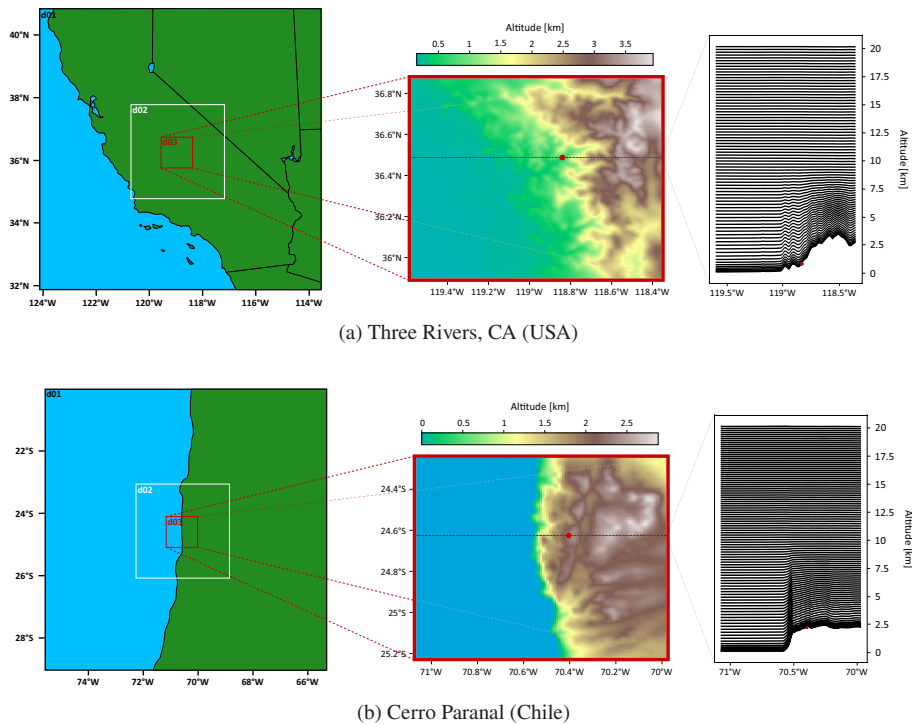


Fig. 2. WRF configurations for simulations conducted at Three Rivers, CA (USA), and Cerro Paranal (Chile). Left part presents the three nested domains, middle part shows the topography of the inner domain, and right part gives the pressure levels distribution. The red dot depicts the exact location where measurements have been collected.

Table 1. Grid parameters for WRF simulations.

Domain	Grid resolution (km)	Number of grid points	Domain size (km)	Number of vertical levels
d01	9	112×112	1008×1008	100
d02	3	112×112	336×336	100
d03	1	112×112	112×112	100

In fact, Table 1 gives the default WRF configuration used in this work. However, some variations have been studied, such as in Section 4.1.3, where the number of vertical levels is modified to monitor its impact on the model performance.

2.2.2. Physical parameterization

The different physical parameterization schemes representing sub-grid processes that have been chosen are: Tiedtke [39] for cumulus physics (only in domain d01), WSM6 [40] for microphysics, Dudhia [41] and RRTM [42] for shortwave and longwave radiations, and revised MM5 [43] for the surface layer. Of particular interest is the MYNN 2.5 [44] scheme used for planetary boundary layer physics, as it enables recording of the turbulent kinetic energy in WRF outputs, useful for the C_n^2 model presented in Section 3.1.

A sensitivity analysis of WRF outputs for OT forecast depending on the chosen physical schemes can be found in [45]. Its application to the locations considered in this paper should be further explored.

3. C_n^2 Models based on meteorological quantities

To obtain OT-related quantities, it is necessary to use a C_n^2 model to translate the simulated meteorological quantities to C_n^2 profiles. This requires a parametric model, that is, a model using meteorological, temporal, or geographical quantities to compute a C_n^2 value. This is the case of the Hufnagel-Valley [2] and HAP [46] models for example, as well as of the Dewan model [47]. On the contrary, non-parametric models provide analytical expressions of C_n^2 profile as a function of the altitude z only, and are mostly derived from empirical mean profiles (e.g., SLC models [48], CLEAR I model [49], etc.). More details about the distinction between parametric and non-parametric models can be found in [32] and [49].

Another common classification of C_n^2 models is based on their origin, either empirical or theoretical [32]. Empirical models are derived based on measurements above a given site, making them simple to use, but site-specific. Instead, theoretical models rely on turbulence theory, and offer a better understanding of the modelled phenomena. For example, this is the case of the Tatarskii model [15] presented in Section 3.2.

Lastly, numerical models are also of interest, especially when relying on NWP simulations to forecast meteorological quantities. Indeed, those are models involving the TKE, solved in fluid mechanics simulations, that can be used to feed a C_n^2 model [21,24,50]. The model presented in Section 3.1 belongs to this category.

3.1. TKE-based model

The first considered C_n^2 model is a parametric and numerical TKE-based model presented in [21]. In recent years, it has been extensively used for OT forecast in astronomy, namely in Astro-Meso-Nh [21,22,51], making it suitable for the optical communication application studied here. This work extends the model and results presented in [21,22,51] by rigorously assessing the TKE model performance during daytime conditions, and comparing its performance with another C_n^2 model.

This model provides the refractive index structure parameter C_n^2 from the temperature structure parameter C_T^2 thanks to the Gladstone's relationship [49]

$$C_n^2 = \left(\frac{80 \times 10^{-6} p}{T^2} \right)^2 C_T^2, \quad (1)$$

where T is the temperature in kelvin, and p is the pressure in hectopascal. This relationship is assumed to be valid for all visible wavelengths [2]. A modified Tatarskii's expression is then

used to obtain C_T^2 from the mixing length L and the square of the potential temperature vertical gradient, that is,

$$C_T^2 = 0.58\phi_3 L^{4/3} \left(\frac{\partial \bar{\theta}}{\partial z} \right)^2, \quad (2)$$

with $\bar{\theta}$ representing the grid-averaged value of the potential temperature [52]. For stable layers, the mixing length L is associated to the Deardoff length [53],

$$L = \sqrt{\frac{2e}{\frac{g}{\theta_v} \frac{\partial \theta_v}{\partial z}}}, \quad (3)$$

where the parameter ϕ_3 is equal to 0.78 [21]. Equation (3) involves the TKE depicted by e , the gravity of Earth g , and the virtual potential temperature θ_v equal to $\theta_v = \theta(1 + 0.61r)$ for unsaturated air, with r depicting the mixing ratio of water vapour.

As a result, meteorological quantities, such as the pressure, p , the temperature, T , the mixing ratio, r , as well as the TKE, e , computed in WRF simulations can directly be fed to Equations (1) to (3) in order to obtain C_n^2 . A similar approach has been presented in [23]. In [50], a calibration of the minimum TKE value depending on the altitude has been presented, and is a possible extension for the model given here.

Examples of C_n^2 profiles computed with this model are given in Section 4.1 and in Figure 3. In the following, it is referred to as the TKE model.

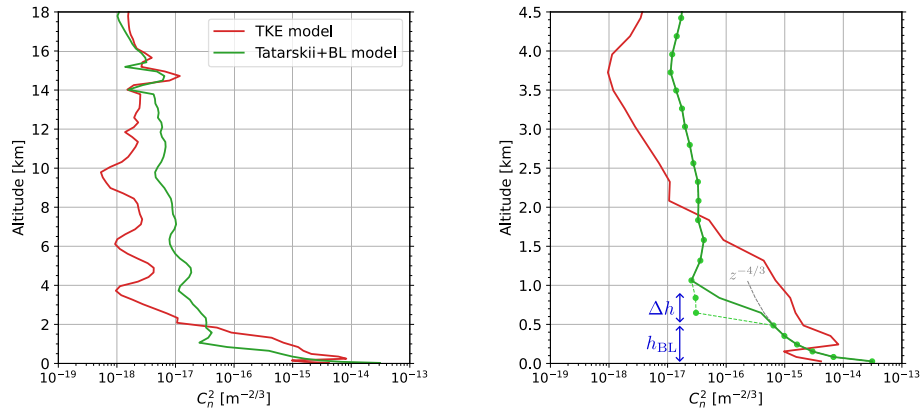


Fig. 3. Modelled C_n^2 profiles at Paranal for March 03, 2023, at 16h00 UTC (13h00 local time, daytime).

3.2. Hybrid Tatarskii model

Beside the numerical TKE-based C_n^2 model, a theoretical model relying on Tatarskii's equation [15] is used,

$$C_{n,\text{Tat}}^2(z) = a^2 L_0^{4/3} M^2, \quad (4)$$

with $a^2 = 2.8$ [54], and $M = \frac{\partial n}{\partial z}$ given by [35]

$$M = -\frac{80 \times 10^{-6} p}{T\theta} \frac{\partial \theta}{\partial z}. \quad (5)$$

It involves the pressure, p , in hectopascal, the temperature, T , in kelvin, the potential temperature, θ , in kelvin, the altitude, z , in meter, and the refractive index, n . The chosen outer

scale, L_0 , model is the HMNSP99 model [47,55], derived from measurements in New Mexico, USA,

$$L_0^{4/3} = 0.1^{4/3} \times 10^Y \text{ with } Y = \begin{cases} 0.362 + 16.728 S - 192.347 \frac{\partial T}{\partial z} & \text{in the troposphere,} \\ 0.757 + 13.819 S - 57.784 \frac{\partial T}{\partial z} & \text{in the stratosphere.} \end{cases} \quad (6)$$

The vertical shear of the horizontal wind velocity, depicted by S , is expressed in meters per second, while the tropopause height, that is, the limit between the troposphere and the stratosphere, depends on the location. With the presented models, M and L_0 are functions of the altitude, z , such that (4) provides a vertical $C_n^2(z)$ profile.

This model has previously been used with TREX radiosonde measurements, and compared with their C_n^2 measurements [56]. However, it has been found to underestimate C_n^2 in the boundary layer, such that, in the following, a hybrid C_n^2 model is suggested [33]. The boundary layer C_n^2 profile is derived from the Monin-Obukhov similarity theory [30,57], giving an estimation of the ground C_n^2 thanks to [58]

$$C_n^2 = A^2 C_T^2 + B^2 C_q^2 + 2ABC_{Tq}, \quad (7)$$

where A is equal to $79 \times 10^{-6} \frac{\rho}{T^2}$, and B to -56.4×10^{-6} [30]. C_T^2 , C_q^2 , and C_{Tq} , are obtained from the temperature scaling parameter T^* and the humidity scaling parameter q^* :

$$C_T^2 = \frac{g_t \left(\frac{z}{L}\right)}{z^{2/3}} T^{*2}, \quad C_q^2 = \frac{g_t \left(\frac{z}{L}\right)}{z^{2/3}} q^{*2}, \quad \text{and} \quad C_{Tq} = \frac{g_t \left(\frac{z}{L}\right)}{z^{2/3}} T^* q^*. \quad (8)$$

They depend on the friction velocity, u^* , the sensible heat flux, SH, the latent heat flux, LH, the density of air, ρ , the specific heat capacity of air at constant pressure, c_p , and the latent heat of vaporization of water, l_v , through [58]

$$T^* = -\frac{\text{SH}}{1.225 u^* c_p (1 + 0.84q)} \quad \text{and} \quad q^* = -\frac{\text{LH}}{u^* \rho l_v}. \quad (9)$$

The quantities u^* , SH, and LH, can be included in WRF simulation outputs, such that T^* and q^* can be computed.

Finally, $g_t \left(\frac{z}{L}\right)$ is the similarity function given by [30,58]

$$g_t \left(\frac{z}{L}\right) = \begin{cases} 4.9 \left(1 - 6.1 \frac{z}{L}\right)^{-2/3}, & \text{for } \frac{z}{L} < 0 (\text{unstable}) \\ 4.9 \left(1 + 2.2 \left(\frac{z}{L}\right)^{2/3}\right), & \text{for } \frac{z}{L} > 0 (\text{stable}) \end{cases} \quad \text{with} \quad \frac{z}{L} = -\frac{0.4 g \text{ SH } z}{1.08 c_p u^{*3} T}. \quad (10)$$

This function gives the vertical evolution of C_T^2 , C_q^2 , and C_{Tq}^2 close to the surface. Assuming those quantities are properly scaled by T^* and q^* , as given in (8), they follow the same vertical dependency, that is, the same similarity function $g_t \left(\frac{z}{L}\right)$ [30].

As a result, Equation (7) evaluated at $z = 2$ meters provides the ground C_n^2 , denoted $C_{n,\text{gr}}^2$. From the C_n^2 ground value, a boundary layer C_n^2 profile is computed up to the boundary layer height h_{BL} using a vertical trend of $z^{-\alpha}$. During daytime, $\alpha = 4/3$ and this trend corresponds to the decrease of C_n^2 in the atmospheric boundary layer dominated by convection. During nighttime, $\alpha = 2/3$ [2]. The implications of the α exponent are further discussed in Section 4.2.3. The boundary layer height, h_{BL} , is a WRF simulation output. The continuity between this boundary layer model and the Tatarskii model is ensured thanks to a linear interpolation, from h_{BL} up to

$h_{BL} + \Delta h$. The final C_n^2 model, referred to as Tatarskii+BL model, is given by [33]

$$C_n^2(z) = \begin{cases} C_{n,gr}^2 \cdot \left(\frac{z}{2}\right)^{-\alpha} & \text{for } z \leq h_{BL}, \\ C_{n,gr}^2 \cdot \left(\frac{h_{BL}}{2}\right)^{-\alpha} \frac{h_{BL} + \Delta h - z}{\Delta h} + C_{n,Tat}^2(z) \frac{z - h_{BL}}{\Delta h} & \text{for } h_{BL} < z \leq h_{BL} + \Delta h, \\ C_{n,Tat}^2(z) & \text{for } z > h_{BL} + \Delta h. \end{cases} \quad (11)$$

In the following, a default value of $\Delta h = 0.2 h_{BL}$ is used. This choice is motivated by the little influence of h_{BL} and Δh that has been observed on the predicted coherence length in Section 4.2. Nevertheless, a quantitative analysis of the impacts of those parameters will be conducted in future work. Figure 3 illustrates the modelled C_n^2 profiles for March 03, 2023, at 16h00 UTC, above the Paranal observatory (see Section 4.2). The right part of the figure focuses on the boundary layer, with $h_{BL} = 550$ m and $\Delta h = 300$ m (set for illustration purposes). The dots and dashed lines highlight the interpolation between the upper part coming from the Tatarskii model, and the lower part coming from the boundary layer model. The smooth vertical trend in $z^{-4/3}$ in the boundary layer can also be identified, further illustrated by the dashed gray line.

4. Validation of the presented approach and C_n^2 models

This section presents the application of the approach presented in Section 2 with the two C_n^2 models from Section 3 to two different locations: Three Rivers, CA (USA), and Paranal observatory, Chile. First, the forecast of meteorological quantities is validated, and then the optical turbulence forecasts are compared with measurements. Table 2 summarizes the measurements available at each location and used for the model validation.

Table 2. Summary of available measurements for the model validation.

Measurement campaign	T-REX	24hSHIMM at Paranal
Location	Three Rivers, CA, USA	Cerro Paranal, Chile
Latitude, Longitude	36.4872°N, 118.84048°W	24.62615°S, 70.40387°W
Altitude	503 m	2625 m
Dates of campaign	20/03/2006 to 06/04/2006	28/02/2023 to 05/03/2023
Meteorological measurements	Yes, from radiosonde	No
C_n^2 profiles	Yes, from thermosonde	No
r_0 measurements	No	Yes, from SHIMM
Daytime/nighttime	8 nighttime profiles, 7 daytime profiles	Continuous, over 6 days

4.1. Comparison with T-REX campaign thermosonde measurements

From 20 March 2006 to 6 April 2006, the Air Force Research Laboratory conducted the T-REX campaign in Sierra Nevada Mountains, near Three Rivers, CA [59]. It consisted in the launches of several radiosondes equipped with thermosondes, hence recording macroscale meteorological parameters, as well as the C_n^2 profile. Data can be accessed online thanks to the Earth Observing Laboratory data archive [60].

The location of the launch site is 36.4872°N, 118.84048°W, having an altitude of 503 m. This is the location depicted by a red dot in Figure 2(a). The radiosondes offer a vertical resolution of 10 meters, approximately constant during the whole flight, and record the altitude, pressure, temperature, wind speed and direction, and the relative humidity. The thermosondes can compute the temperature structure function C_T^2 from measurements of two temperature sensors spaced by one meter. Then, C_n^2 is obtained from C_T^2 using (1). In total, 15 flights have been exploited, 8

being associated to nighttime conditions and 7 to daytime conditions (see Appendix A). The measured profiles have been binned using a vertical distance of 100 m for the comparison with the modelled profiles.

4.1.1. Meteorological parameters

As a first step, a comparison between the measured meteorological parameters and the simulated ones using WRF is conducted. WRF simulations are initialized at least 6 hours prior to the radiosonde launch time, and outputs at the same instants of the radiosonde launches are recorded.

The left part of Figure 4 depicts the average temperature and wind speed profiles over the 15 flights, computed either from the radiosonde measurements or from the WRF simulations. The shaded areas show the average profiles plus or minus their standard deviations, with the shaded areas delimited by dashed lines associated to the measurements. Good agreement is achieved, especially for the temperature in the troposphere (below ~10 km of altitude), which is important for further C_n^2 modelling. Wind speed fluctuations in the measurements are observed, and partially modelled in WRF simulations. Those agreements are quantified on the right part of Figure 4 using the absolute bias and the root-mean-square error (RMSE), defined as

$$\text{Absolute bias} = \sum_{i=1}^N \frac{|Y_i - X_i|}{N}, \quad (12)$$

$$\text{RMSE} = \sqrt{\sum_{i=1}^N \frac{(Y_i - X_i)^2}{N}}, \quad (13)$$

with N being the number of measurements ($N = 15$), X_i the i -th measurement of the temperature (resp. wind speed) profile, and Y_i the modelled temperature (resp. wind speed) profile. Those quantities depend on the altitude, z , such that their vertical profiles can be analysed [61]. They show that most temperature differences are located close to the ground, as well as at high altitude. The error on the wind speed profile is roughly constant in the troposphere, and starts to increase for altitudes higher than 12 km.

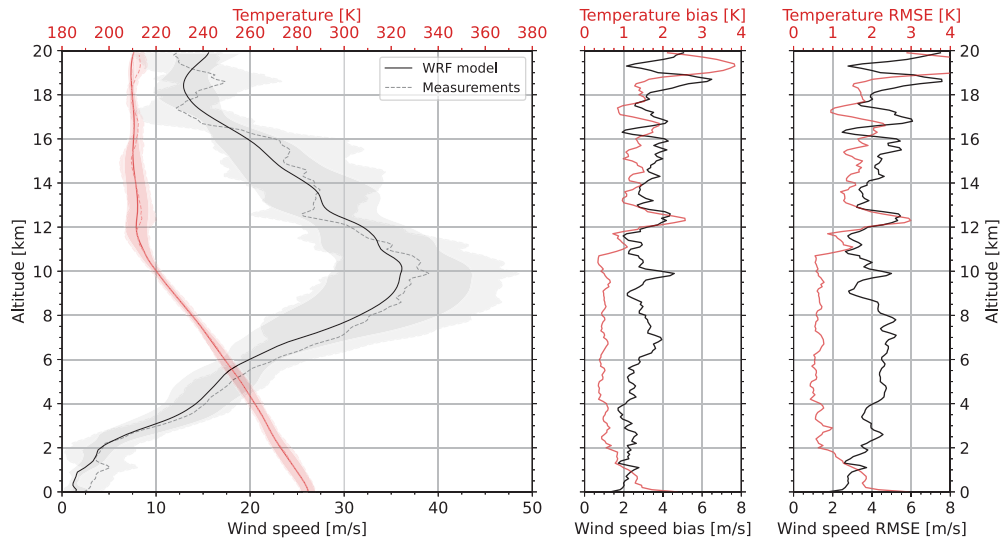


Fig. 4. Average temperature and wind speed profiles for T-REX campaign (left), and associated absolute bias and RMSE (right).

4.1.2. C_n^2 profiles

Figure 5 provides the temperature and wind speed measurements and forecasts for T-REX019 flight (right part). On the left part of the figure, a comparison between the modelled C_n^2 profiles and the measured one is conducted. The tropopause height is set to 12 km for the Tatarskii+BL model, as it approximately corresponds to the altitude where the average temperature profile stops decreasing with the altitude (Figure 4).

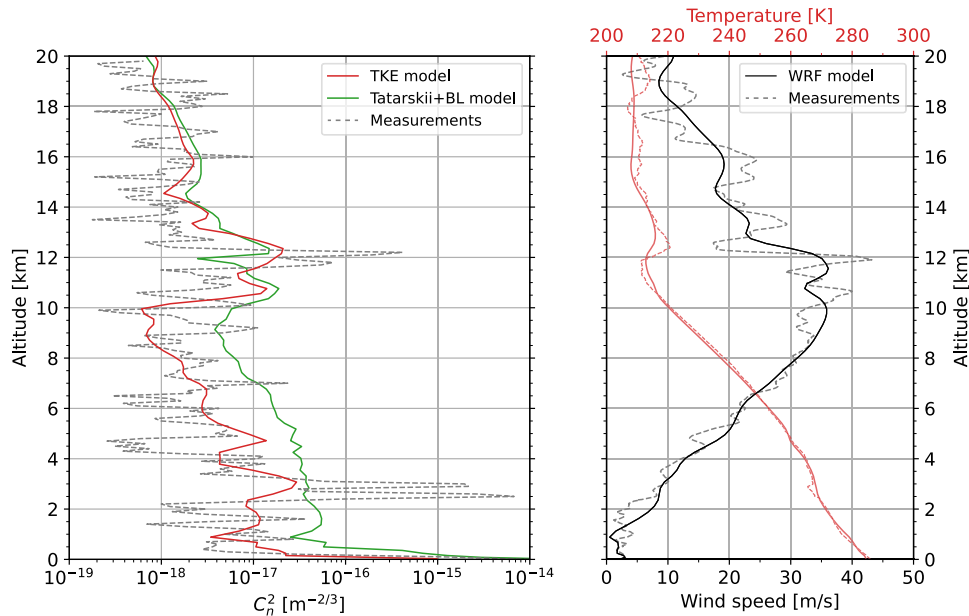


Fig. 5. C_n^2 , temperature, and wind speed profiles on March 31, 2006 at 00h48 UTC (March 20, 2006 at 16h48 in local time - daytime - T-REX019).

In Figure 5, the general shape and magnitude of the C_n^2 profile is well modelled by the TKE model, while the Tatarskii+BL model tends to overestimate the turbulence in the troposphere. Moreover, two large turbulent layers can be identified in the measurements, and are associated with temperature inversion layers. They are also modelled by the TKE model, even though their magnitudes underestimate the measured values.

The average of all 15 profiles is presented on the left part of Figure 6, with all individual profiles given in Appendix A. The shaded areas represent the average plus or minus the standard deviation, computed from the logarithm in base 10 of the C_n^2 profiles. Furthermore, the absolute bias and RMSE are given in the right part of the figure, using (12) and (13) applied on $\log_{10}(C_n^2)$.

Average trends are well described by both models, even though the TKE model seems to underestimate the turbulence below 5 km of altitude. On the contrary, the Tatarskii+BL model overestimates C_n^2 in the boundary layer.

As seen by the shaded areas in Figure 6, both models show smaller standard deviations than the measurements, except for the TKE model around 7 km of altitude. Indeed, there is a peak in the average C_n^2 profile, associated to large C_n^2 values monitored during the flight T-REX039 (see Appendix A). This peak is also present in the TKE model, but is neglected by the Tatarskii+BL model. The TKE model also represents other localized turbulent layers, despite underestimating them, as previously observed in Figure 5.

The absolute bias and RMSE metrics tend to confirm that most discrepancies are observed close to the ground, and at the tropopause altitude (~ 10 km). Above 15 km, both models converge

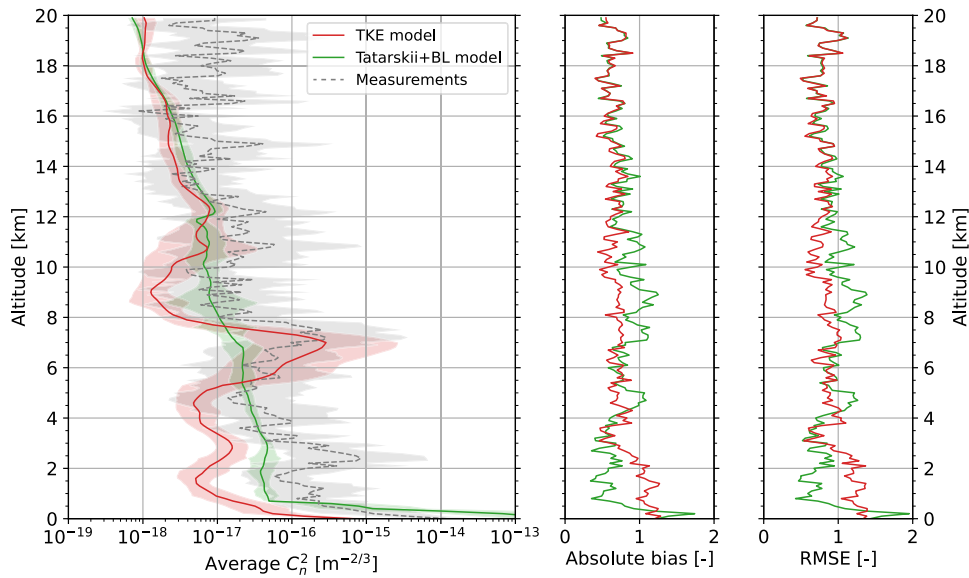


Fig. 6. Average C_n^2 profiles over the 15 T-REX flights (left), and associated absolute bias and RMSE (right).

to the same average C_n^2 values. Average values of the absolute bias (respectively RMSE) over all altitudes is 0.71 (resp. 0.86) for the TKE model, and 0.75 (resp. 0.90) for the Tatarskii+BL model.

4.1.3. Impact of the number of vertical levels used in WRF simulations

To conclude the comparison between T-REX thermosonde measurements and the modelled profiles, a study of the impact of the number of vertical levels used in the WRF simulations is conducted. In this case, the centered absolute bias and centered RMSE on $\log_{10}(C_n^2)$ are monitored. The centering comes from removing the mean C_n^2 profile over the 15 flights prior to the computation of the absolute bias and the RMSE. This eliminates the average bias between the measured and modelled profiles that does not vary with the number of vertical levels. Therefore, the centered metrics enable improved insight into how small C_n^2 fluctuations with altitude are better depicted with the addition of more vertical levels, disregarding the differences on the average profiles.

The evolution of those two metrics, averaged over all altitudes from 0 to 20 km, is represented in Figure 7, for different numbers of levels (the larger the number of levels, the longer the computation time). In this figure, there seems to be a limit to the achievable decrease of centered absolute bias and RMSE that is obtained by increasing the number of vertical levels, starting around 80 to 100 levels. This is particularly true for the TKE model, while the decrease is smaller for the Tatarskii+BL model. This result motivates the choice of 100 vertical levels used in this study. However, such findings are currently limited to the T-REX campaign case (15 flights), and should be further studied for other locations. More measurements and metrics should be monitored in order to determine which parts of the atmosphere are better represented when increasing the number of vertical levels.

4.2. Comparison with continuous measurements of Fried parameter at Paranal

The Fried parameter measurements at Paranal observatory were carried out over a period of six days from 28th February to March 5th 2023 using a 24-hour Shack-Hartmann Image Motion

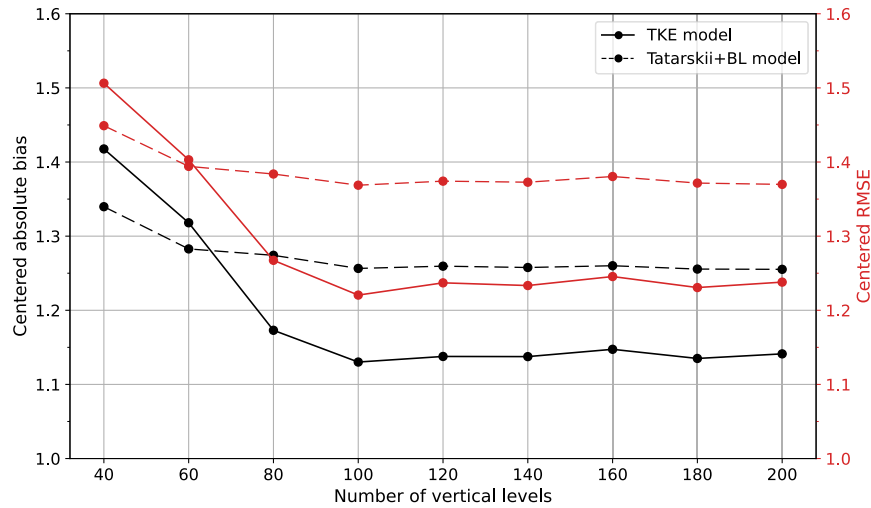


Fig. 7. Evolution of centered absolute bias and RMSE with the number of WRF vertical levels.

Monitor (24hSHIMM), developed by Durham’s Centre for Advanced Instrumentation. The 24hSHIMM is a portable 30 cm telescope equipped with a Shack-Hartmann wavefront sensor. It observes stars in the near-infrared, which limits sky background noise and strong turbulence during daytime, and measures statistical fluctuations in both the phase and intensity resulting from OT to provide fully continuous measurements of a low-resolution vertical OT profile. Estimates of the Fried parameter are obtained directly from this profile; the full description of the instrument and its working principle can be found in [12]. The measurements at Paranal include two full nights of data collected during the initial stage of the campaign, followed by four nights and three days of continuous operation. The 24hSHIMM was mounted on a concrete pier with no dome, approximately 2 m above the ground in the North-Western corner of the site. Instead of the standard design utilising an InGaAs camera, the system was operated with a ZWO ASI174MM CMOS camera. As a result, the effective wavelength was determined to be approximately 695 nm. This increased the minimum threshold of reliable r_0 measurements as determined by simulation to approximately 1.5 cm at a wavelength of 500 nm, therefore measurements below this have been excluded from this analysis. All measured parameters displayed below have been corrected to zenith and for a wavelength of 500 nm.

4.2.1. Temporal evolution of Fried parameter

In this study, the continuous measurement of the Fried parameter r_0 by the 24hSHIMM instrument is of great interest to validate the daytime and nighttime applications of the presented models. From modelled C_n^2 profiles above the location of Paranal (that is, at the center of the WRF simulation domain), the Fried parameter is computed using its analytical expression in the case of plane waves [4]

$$r_0 = \left(0.423 k^2 \sec(\xi) \int_{h_0}^{\infty} C_n^2(z) dz \right)^{-3/5}, \quad (14)$$

where ξ is the elevation angle measured from zenith ($\xi=0^\circ$ in the following), and $k = 2\pi/\lambda$ is the wavenumber (λ is the wavelength, $\lambda=500$ nm in this case). Finally, h_0 is the starting altitude for the C_n^2 profile integration, chosen as the first level in WRF simulations, that is approximately located 20 meters above the ground. As seen from (14), the Fried parameter is dominated by large value of C_n^2 in its profile, arising mostly in the boundary layer. As a result, Fried parameter

measurements are useful to assess the validity of the boundary layer profiles from both C_n^2 models. From observations of the average temperature profile at Paranal, the tropopause altitude is set to 14 km for the Tatarskii+BL model.

WRF simulations are conducted using the parameterization presented in Section 2, centred on Paranal observatory (24.62615°S, 70.40387°W, altitude of 2625 m). A six-hour lead time is ensured by initializing the simulations with the data at 18h00 UTC the day before, and recording the meteorological outputs every 5 minutes from midnight to midnight the next day. Hence, two time series of the predicted Fried parameter, simulated day by day, are obtained, one for each C_n^2 model.

Figure 8 presents the temporal evolution of the measured Fried parameter r_0 using blue dots. Its associated uncertainty, typically small, is depicted by the vertical blue bars. The red curve gives the forecast r_0 parameter from the TKE model, while the green curve corresponds to the forecast using the Tatarskii+BL model. Gray areas depict nighttime at Paranal, defined by civil twilight. This figure leads to several observations and comments:

1. The 24h variation of r_0 is clearly identified in the measurements. Indeed, during daytime, r_0 is low (as low as 2 cm), while it is larger in nighttime, when it can reach up to 30 cm. This nighttime-daytime variation is well-modelled by both C_n^2 models.
2. The TKE model seems to agree well with the measurements (nighttime and daytime), even though it suffers from oscillations not observed in the measurements.
3. The Tatarskii+BL model especially fits with measurements during nighttime. However, it tends to overestimate daytime r_0 (hence underestimating daytime turbulence in the C_n^2 profile). As seen from the distributions in Figure 10, it tends to predict realistic values, but not at the right times.
4. The daytime-nighttime shift in the Tatarskii+BL model leads to peaks in the predicted r_0 . Those have been associated to transitions of the sensible heat flux, SH, from negative values to positive values (and vice-versa). Such important transitions are also observed in [58] for the ground C_n^2 value.
5. A small discontinuity in the r_0 predictions is sometimes observed at midnight UTC, as it corresponds to the transition between two consecutive WRF simulations.

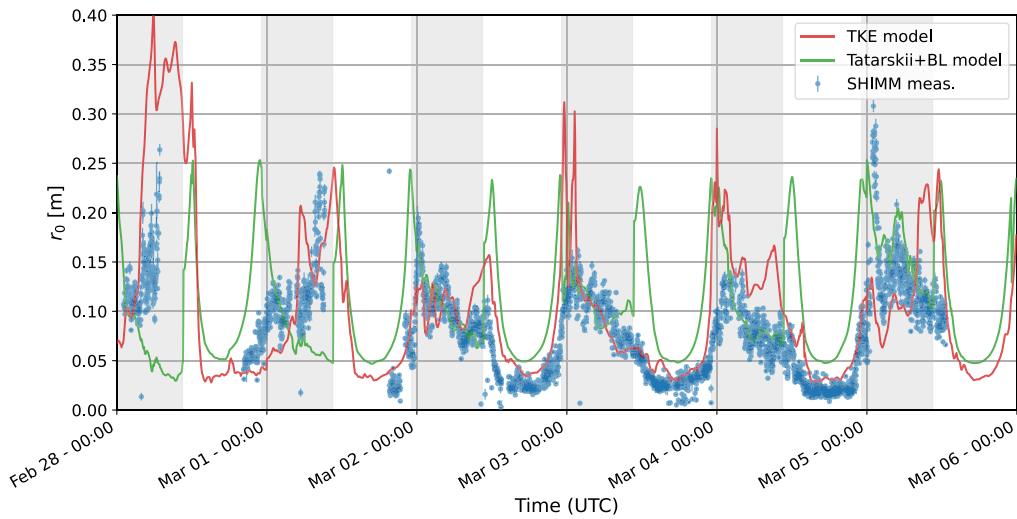


Fig. 8. Continuous measurements of Fried parameter at Paranal for 6 consecutive days, compared with the prediction from each C_n^2 model (using (14), with $h_0 = 20$ m).

The overestimation of r_0 by the Tatarskii+BL model can be mitigated by modifying the exponent α in (11). For example, a daytime exponent of 1, instead of $4/3$ as detailed in Section 3.2, has been found to visually improve the agreement with the measurements during daytime. A quantitative study of the daytime exponent variation is conducted in Section 4.2.3.

4.2.2. Correlations and distributions

By binning r_0 measurements in 5-minute bins, a comparison with forecast r_0 at the same instants can be conducted. It leads to the correlation plots presented in Figure 9, where dark dots are associated to daytime, while light squares correspond to nighttime. Distributions of the measurements and the predictions are represented in Figure 10, separating the daytime and nighttime conditions.

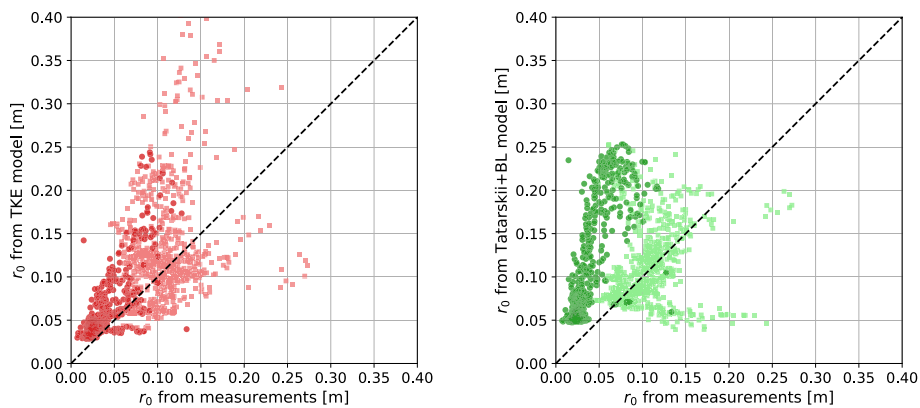


Fig. 9. Correlation between measured and predicted Fried parameters (using (14), with $h_0 = 20$ m). Left: TKE model, right: Tatarskii+BL model. Dark dots are associated to daytime, while light squares correspond to nighttime.

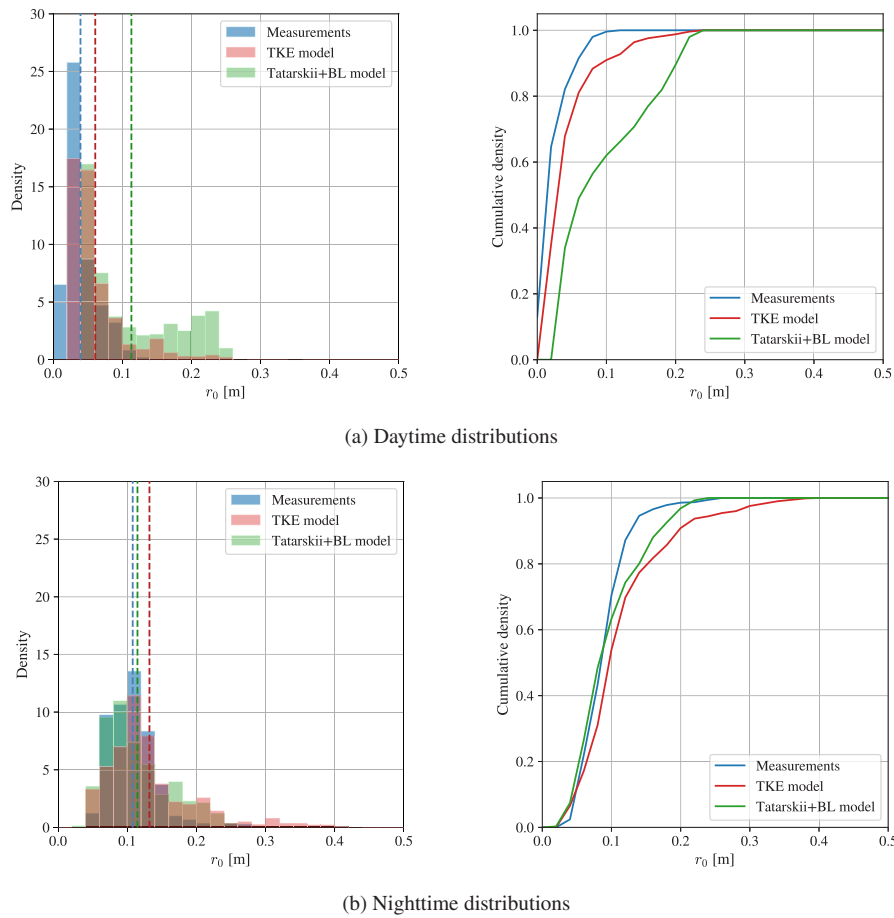


Fig. 10. Distributions (density and cumulative density) of measured and predicted Fried parameters.

TKE model Regarding the TKE model, good prediction capabilities for low r_0 are observed on the correlation plot, with a larger spread for large r_0 values. A correlation coefficient of 0.59 is recorded, between the 5-minute measurements and predictions. The associated RMSE is 5.8 cm.

However, considering only daytime measurements and forecast, the correlation coefficient reaches 0.75, with a RMSE of 3.4 cm. The daytime distribution in Figure 10(a) shows good agreement with the distribution of the measurements. It also emphasizes the lack of small predicted r_0 values from the TKE model, hence shifting the distribution slightly to the right.

For nighttime conditions, the correlation coefficient is 0.22, and the RMSE is 7 cm. This large RMSE comes from the overestimation of r_0 during the night, especially for February 28. This also impacts the tail of the distribution in Figure 10(b).

The overestimation of the Fried parameter during daytime (associated to the underestimation of the C_n^2 profile especially in the boundary layer), as well as the large peaks in r_0 during nighttime, have been related to an underestimation of the TKE in the boundary layer. Further investigations will focus on improving the parameterization of the boundary layer in WRF but will require access to meteorological data not available for this study. Model improvements by modifying the surface layer parametrization in the NWP software have been demonstrated in the literature [62].

Tatarskii+BL model In the correlation plot of the Tatarskii+BL model (Figure 9), two main clusters can be identified, related to daytime or nighttime predictions: the one following the equality line (nighttime), and a cluster of points overestimating r_0 , located to the left of the equality line (daytime). The global correlation coefficient is 0.24, while the RMSE is 7.2 cm.

In daytime only, the correlation coefficient is 0.76, showing that the daytime variations are well depicted, up to a proportionality factor. Indeed, the daytime cluster in Figure 9 has actually an average slope close to 3 (empirical observation) instead of one, meaning that daytime r_0 predictions from the Tatarskii+BL model overestimate the measurements in a consistent manner, explaining the large correlation coefficient. The RMSE is larger, being equal to 9.0 cm, and comes from the peaks at the beginning and the end of the day, as well as from the general overestimation of r_0 (see Figure 8). The latter also impacts the distribution presented in Figure 10(b). This overall overestimation of the Fried parameter during daytime could originate from a slight underestimation of the sensible heat flux in the boundary layer.

In nighttime, the correlation is 0.11, and the RMSE is 5.6 cm. However, the agreement between the predicted and measured distributions is good, as seen from Figure 10(b). This shows that, even if the Tatarskii+BL model does not predict the correct r_0 at the right time, it provides realistic values of r_0 in agreement with the distribution of the measurements.

4.2.3. Study of daytime exponent

The daytime exponent α , in (11), influences the overall performance of the Tatarskii+BL model. According to the literature, it should be set to $4/3$, even though some previous studies showed that, over complex terrains such as mountainous areas, an exponent of $1/3$ can be found [2]. In order to assess its influence on the r_0 predictions, daytime correlation coefficients and RMSE have been monitored for several values of the exponent. Results are presented in Figure 11.

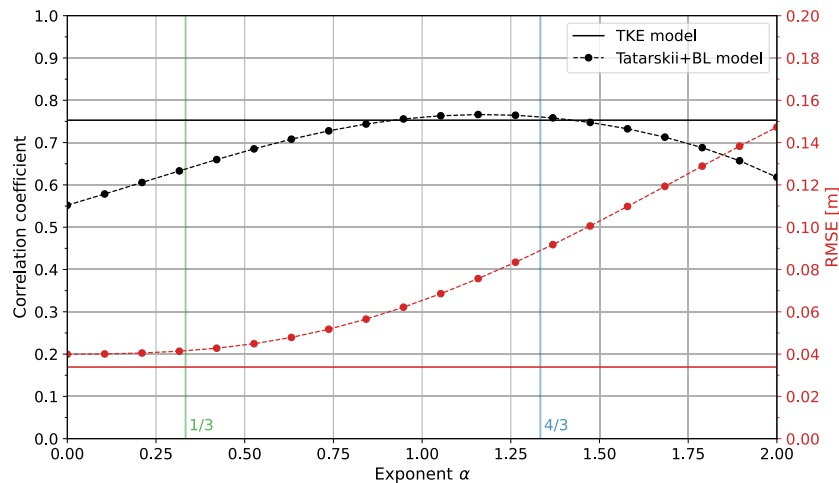


Fig. 11. Sensitivity analysis to daytime exponent α of Tatarskii+BL model. TKE model is also represented for reference. Daytime only correlation coefficients and RMSEs depicted on the graph.

Interestingly, the correlation coefficient is maximized for daytime exponents between 1 and $4/3$, that is, those exponents are the best to model the daytime variations of seeing. This motivates the choice of using the literature value of $4/3$ for α (see Section 3.2). Nevertheless, large daytime exponents tend to lead to overestimations of r_0 , increasing the RMSE as seen in Figure 11.

5. Conclusion

A general approach to perform OT forecast has been presented, relying on numerical weather predictions and involving two different C_n^2 models (TKE model and Tatarskii+BL model). The main motivation behind this approach and the associated C_n^2 models is its applicability to optical communication sites for nighttime and daytime predictions.

While compared with thermosonde measurements, both C_n^2 models show similar performance for the prediction of vertical C_n^2 profiles in the free atmosphere, with the TKE model identifying most of the isolated turbulent layers. Regarding the modelling of the boundary layer, a comparison with measurements of the coherence length at Paranal observatory shows that both models offer rather complementary performance and enables to identify their current limitations. Indeed, relative daytime variations are well depicted in the TKE and the Tatarskii+BL model, with correlations larger than 0.75. The magnitude of the boundary layer is underestimated in both models, and especially in the Tatarskii+BL model, such that the predicted daytime distributions do not agree with the measurements for large r_0 values. For nighttime, the predicted values agree very well in distributions, particularly for the Tatarskii+BL model. However, correlations with the measurements is relatively poor, highlighting a temporal mismatch between the predictions and the measurements.

This work highlights the difficulty of accurately predicting the boundary layer in the C_n^2 modelling, that is required for daytime forecasts. Current limitations and biases have been related to the estimations of the TKE in the boundary layer and of the sensible heat flux. Further improvements of the modelling of those parameters will require accurate measurements of the meteorological quantities in the boundary layer at the locations of future optical communication sites, as well as long-term measurement campaigns of OT parameters. Daytime and nighttime measurements will be of interest to assess the quality of the sites.

In the future, as short-term forecast remains particularly challenging, alternative approaches combining real-time measurements and forecasts will be explored.

A. Measured and modelled profiles for all T-REX flights

The description of the launching conditions during the T-REX campaign can be found in [59]. Table 3 summarizes the launch times of the different flights, highlighting the ones associated to daytime or nighttime conditions (civil twilight definition). In total, 7 profiles have been measured during daytime conditions, while 8 profiles have been acquired during nighttime.

The measured temperature, wind speed, and C_n^2 profiles for all flights are available in Figures 12 and 13. The corresponding modelled profiles are also depicted in those figures.

Table 3. Launch times of T-REX flights.

Flight ID	Launch time (UTC)	Launch time (local time)	Daytime/nighttime
T-REX004	22/03/2006 02:07	21/03/2006 18:07	Daytime
T-REX005	23/03/2006 02:18	22/03/2006 18:18	Daytime
T-REX006	23/03/2006 02:19	22/03/2006 18:19	Daytime
T-REX007	25/03/2006 05:50	24/03/2006 21:50	Nighttime
T-REX009	25/03/2006 07:53	24/03/2006 23:53	Nighttime
T-REX011	25/03/2006 09:47	25/03/2006 01:47	Nighttime
T-REX012	25/03/2006 09:57	25/03/2006 01:57	Nighttime
T-REX017	28/03/2006 03:47	27/03/2006 19:47	Nighttime
T-REX019	31/03/2006 00:48	30/03/2006 16:48	Daytime
T-REX021	31/03/2006 02:52	30/03/2006 18:52	Nighttime
T-REX029	03/04/2006 00:02	02/04/2006 17:02	Daytime
T-REX031	03/04/2006 01:51	02/04/2006 18:51	Daytime
T-REX039	06/04/2006 01:40	05/04/2006 18:40	Daytime
T-REX040	06/04/2006 03:27	05/04/2006 20:27	Nighttime
T-REX041	06/04/2006 05:14	05/04/2006 22:14	Nighttime

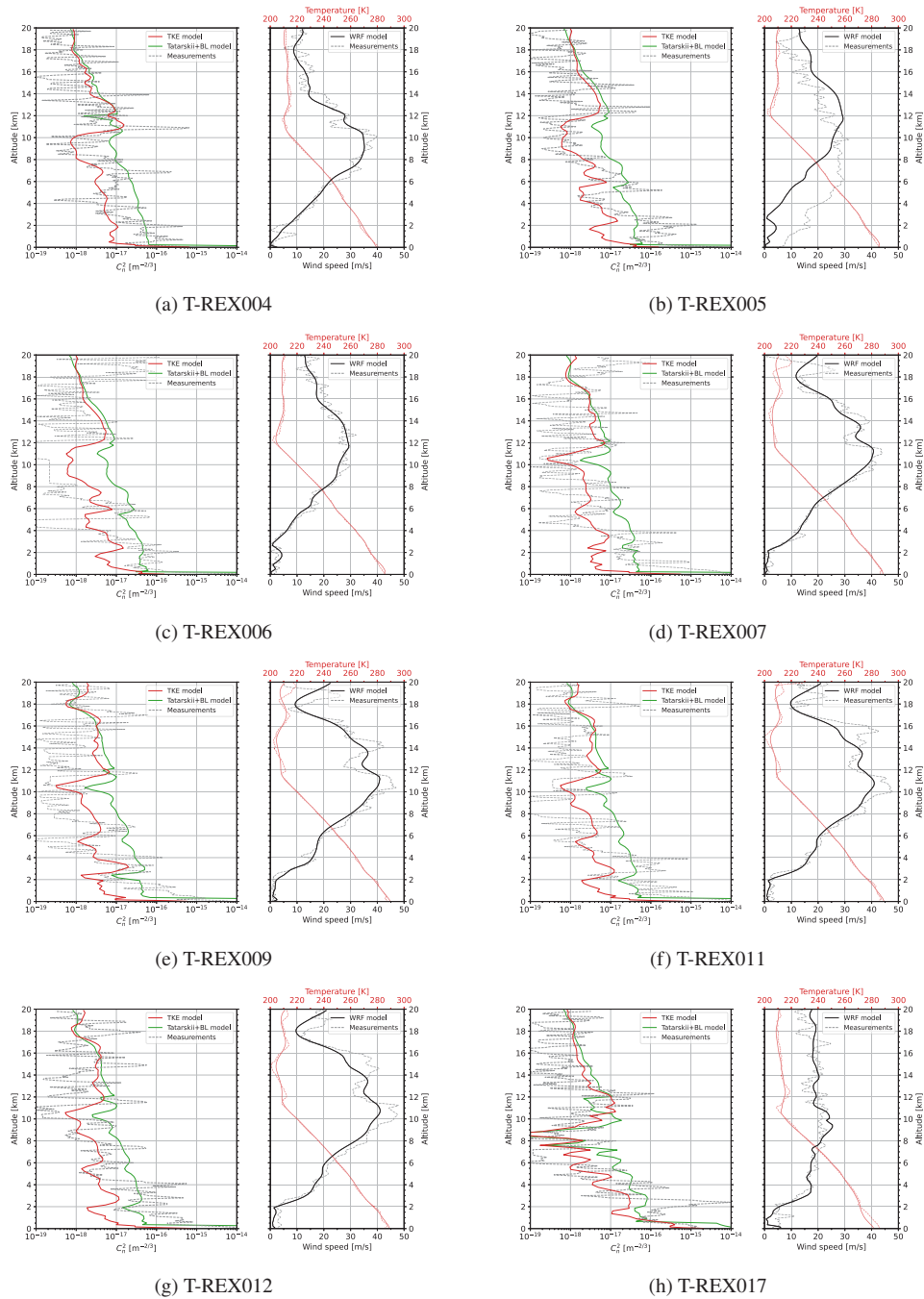


Fig. 12. T-REX flights - Part I.

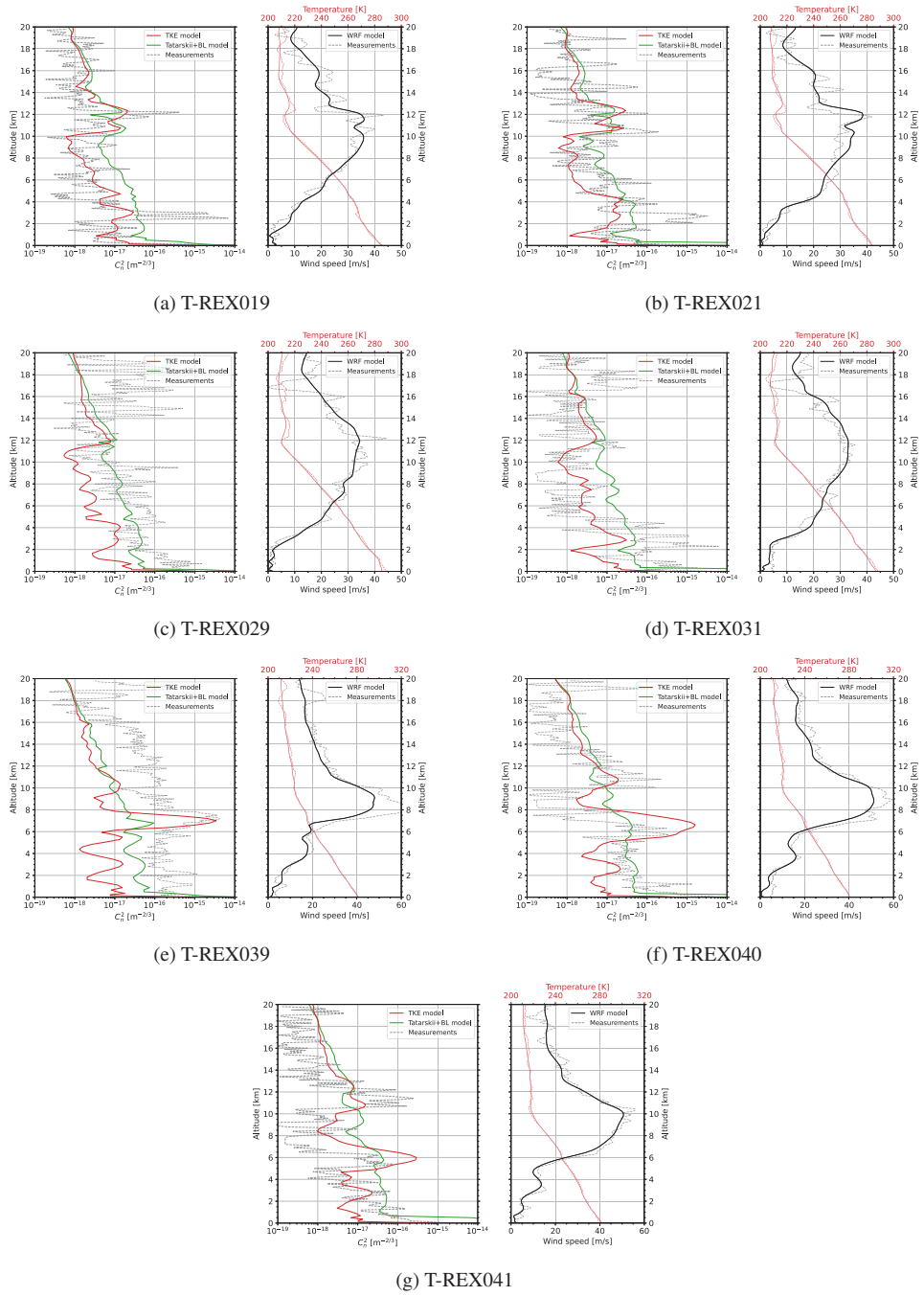


Fig. 13. T-REX flights - Part II.

Funding. Science and Technology Facilities Council (2419794); UK Research and Innovation (MR/S035338/1).

Acknowledgments. AFRL and NCAR are thanked for the access to thermosonde data from the T-REX campaign. Data provided by NCAR/EOL under the sponsorship of the National Science Foundation, <https://data.eol.ucar.edu/>.

Disclosures. The authors declare no conflicts of interest.

Data availability. T-REX thermosonde data are publicly available in [60]. 24hSHIMM measurements at Paranal may be obtained upon reasonable request to ryan.griffiths@durham.ac.uk.

References

1. J. W. Hardy, *Adaptive Optics for Astronomical Telescopes*, vol. 16 (Oxford University Press on Demand, 1998).
2. L. C. Andrews and R. L. Phillips, *Laser Beam Propagation through Random Media, Second Edition* (SPIE Press, 2005).
3. G. B. CCSDS, “Real-time weather and atmospheric characterization data,” Informational Report, CCSDS (2017).
4. F. Roddier, “V The effects of atmospheric turbulence in optical astronomy,” in *Progress in Optics*, vol. 19 (Elsevier, 1981), pp. 281–376.
5. M. Sarazin and F. Roddier, “The eso differential image motion monitor,” *Astronomy and Astrophysics*, **227**, 294–300 (1990).
6. J. Vernin and C. Munoz-Tunon, “Measuring astronomical seeing: the DA/IAC DIMM,” *Publ. Astron. Soc. Pac.* **107**, 265 (1995).
7. A. Tokovinin, “From differential image motion to seeing,” *Publ. Astron. Soc. Pac.* **114**(800), 1156–1166 (2002).
8. A. Rocca, F. Roddier, and J. Vernin, “Detection of atmospheric turbulent layers by spatiotemporal and spatioangular correlation measurements of stellar-light scintillation,” *J. Opt. Soc. Am.* **64**(7), 1000–1004 (1974).
9. J. Osborn, R. Wilson, and M. Sarazin, *et al.*, “Optical turbulence profiling with Stereo-SCIDAR for VLT and ELT,” *Mon. Not. R. Astron. Soc.* **478**(1), 825–834 (2018).
10. R. W. Wilson, “SLODAR: measuring optical turbulence altitude with a Shack–Hartmann wavefront sensor,” *Mon. Not. R. Astron. Soc.* **337**(1), 103–108 (2002).
11. T. Butterley, R. W. Wilson, and M. Sarazin, “Determination of the profile of atmospheric optical turbulence strength from SLODAR data,” *Mon. Not. R. Astron. Soc.* **369**(2), 835–845 (2006).
12. R. Griffiths, J. Osborn, O. Farley, T. Butterley, M. J. Townson, and R. Wilson, “Demonstrating 24-hour continuous vertical monitoring of atmospheric optical turbulence,” *Opt. Express* **31**(4), 6730–6740 (2023).
13. A. Tokovinin, “Measurement of turbulence profile from defocused ring images,” *Mon. Not. R. Astron. Soc.* **502**(1), 794–808 (2021).
14. A. Ziad, C. Giordano, and A. Aresta, *et al.*, “ANAtOLIA: a new mobile site-testing station for astronomy and optical communications,” in *Adaptive Optics Systems VIII*, vol. 12185 (SPIE, 2022), pp. 1877–1887.
15. V. I. Tatarskii, “The effects of the turbulent atmosphere on wave propagation,” Jerusalem: Israel Program for Scientific Translations (1971).
16. J. Osborn and M. Sarazin, “Atmospheric turbulence forecasting with a general circulation model for Cerro Paranal,” *Mon. Not. R. Astron. Soc.* **480**(1), 1278–1299 (2018).
17. C. Qing, X. Wu, X. Li, T. Luo, C. Su, and W. Zhu, “Mesoscale optical turbulence simulations above Tibetan Plateau: first attempt,” *Opt. Express* **28**(4), 4571–4586 (2020).
18. A. Rafalimanana, C. Giordano, A. Ziad, and E. Aristidi, “Prediction of atmospheric turbulence by means of WRF model for optical communications,” in *International Conference on Space Optics—ICSO 2020*, vol. 11852 (International Society for Optics and Photonics, 2021).
19. H. Trinquet and J. Vernin, “A statistical model to forecast the profile of the index structure constant C_N^2 ,” *Environ. Fluid Mech.* **7**(5), 397–407 (2007).
20. C. Giordano, J. Vernin, H. Trinquet, and C. Muñoz-Tuñón, “Weather Research and Forecasting prevision model as a tool to search for the best sites for astronomy: application to La Palma, Canary Islands,” *Mon. Not. R. Astron. Soc.* **440**(3), 1964–1970 (2014).
21. E. Masciadri, J. Vernin, and P. Bougeault, “3D mapping of optical turbulence using an atmospheric numerical model-I. a useful tool for the ground-based astronomy,” *Astron. Astrophys. Suppl. Ser.* **137**(1), 185–202 (1999).
22. E. Masciadri, F. Lascaux, A. Turchi, and L. Fini, “Optical turbulence forecast: ready for an operational application,” *Mon. Not. R. Astron. Soc.* **466**(1), 520–539 (2017).
23. R. J. Alliss and B. D. Felton, “Numerical simulations of optical turbulence using an advanced atmospheric prediction model: Implications for adaptive optics design,” in *Proceedings of the Advanced Maui Optical and Space Surveillance Technologies Conference* (2014), pp. 9–12.
24. S. Basu, J. Osborn, P. He, and A. DeMarco, “Mesoscale modelling of optical turbulence in the atmosphere: the need for ultrahigh vertical grid resolution,” *Mon. Not. R. Astron. Soc.* **497**(2), 2302–2308 (2020).
25. R. Lyman, T. Cherubini, and S. Businger, “Forecasting seeing for the Maunakea Observatories,” *Mon. Not. R. Astron. Soc.* **496**(4), 4734–4748 (2020).
26. C. Robert, M.-T. Velluet, E. Masciadri, A. Turchi, J.-M. Conan, N. Védrenne, G. Artaud, and B. Benammar, “Characterization of the turbulent atmospheric channel of space-ground optical links with parametric models: description and cross-validation with mesoscale models and in situ measurements,” in *Environmental Effects on Light Propagation and Adaptive Systems II*, vol. 11153 (SPIE, 2019), pp. 15–26.

27. N. Vedrenne, C. Petit, and A. Montmerle-Bonnefois, *et al.*, "Performance analysis of an adaptive optics based optical feeder link ground station," in *International Conference on Space Optics—ICSO 2020*, vol. 11852 (SPIE, 2021), pp. 527–535.
28. D. Sadot and N. S. Kopeika, "Forecasting optical turbulence strength on the basis of macroscale meteorology and aerosols: models and validation," *Opt. Eng.* **31**(2), 200–212 (1992).
29. S. Bendersky, N. S. Kopeika, and N. Blaunstein, "Atmospheric optical turbulence over land in middle east coastal environments: prediction modeling and measurements," *Appl. Opt.* **43**(20), 4070–4079 (2004).
30. E. L. Andreas, "Estimating C_n^2 over snow and sea ice from meteorological data," *J. Opt. Soc. Am. A* **5**(4), 481–495 (1988).
31. A. Tunick, "CN2 model to calculate the micrometeorological influences on the refractive index structure parameter," *Environ. Model. & Softw.* **18**(2), 165–171 (2003).
32. F. Quatresooz, G. Orban de Xivry, O. Absil, D. Vanhoenacker-Janvier, and C. Oestges, "Challenges for optical turbulence characterization and prediction at optical communication sites," in *International Conference on Space Optics* (2022).
33. F. Quatresooz, D. Vanhoenacker-Janvier, and C. Oestges, "Daytime forecast of optical turbulence for optical communications," in *Communication and Observation through Atmospheric Turbulence (COAT) workshop* (2023).
34. E. Masciadri, G. Martelloni, and A. Turchi, "Filtering techniques to enhance optical turbulence forecast performances at short time-scales," *Mon. Not. R. Astron. Soc.* **492**(1), 140–152 (2020).
35. T. Cherubini, S. Businger, and R. Lyman, "Modeling optical turbulence and seeing over Mauna Kea: Verification and algorithm refinement," *J. Appl. Meteorol. Climatol.* **47**(12), 3033–3043 (2008).
36. Copernicus Climate Change Service, Climate Data Store, "ERA5 hourly data on pressure levels from 1940 to present," (2023). Copernicus Climate Change Service (C3S) Climate Data Store (CDS), DOI: 10.24381/cds.bd0915c6 (Accessed on 02-05-2023).
37. W. C. Skamarock, J. B. Klemp, J. Dudhia, D. O. Gill, Z. Liu, J. Berner, and X.-y. Huang, "A Description of the Advanced Research WRF Model Version 4," (2019). (No. NCAR/TN-556+STR). <http://dx.doi.org/10.5065/1dfh-6p97>.
38. B. D. Felton, P. D. Hayes, and R. J. Alliss, "Improved atmospheric characterization for free-space link analysis using numerical weather prediction," in *Atmospheric Propagation IX*, vol. 8380 (SPIE, 2012), pp. 99–108.
39. C. Zhang, Y. Wang, and K. Hamilton, "Improved representation of boundary layer clouds over the southeast Pacific in ARW-WRF using a modified Tiedtke cumulus parameterization scheme," *Mon. Weather Rev.* **139**(11), 3489–3513 (2011).
40. S.-Y. Hong and J.-O. J. Lim, "The WRF single-moment 6-class microphysics scheme (WSM6)," *Asia-Pacific Journal of Atmospheric Sciences* **42**, 129–151 (2006).
41. J. Dudhia, "Numerical study of convection observed during the winter monsoon experiment using a mesoscale two-dimensional model," *J. Atmos. Sci.* **46**(20), 3077–3107 (1989).
42. E. J. Mlawer, S. J. Taubman, P. D. Brown, M. J. Iacono, and S. A. Clough, "Radiative transfer for inhomogeneous atmospheres: RRTM, a validated correlated-k model for the longwave," *J. Geophys. Res.: Atmos.* **102**(D14), 16663–16682 (1997).
43. P. A. Jiménez, J. Dudhia, J. F. González-Rouco, J. Navarro, J. P. Montávez, and E. García-Bustamante, "A revised scheme for the WRF surface layer formulation," *Mon. Weather Rev.* **140**(3), 898–918 (2012).
44. M. Nakanishi and H. Niino, "Development of an improved turbulence closure model for the atmospheric boundary layer," *J. Meteorol. Soc. Jpn. Ser. II* **87**(5), 895–912 (2009).
45. A. Rafalimanana, C. Giordano, A. Ziad, and E. Aristidi, "Optimal prediction of atmospheric turbulence by means of the Weather Research and Forecasting model," *Publ. Astron. Soc. Pac.* **134**(1035), 055002 (2022).
46. L. C. Andrews, R. L. Phillips, D. Wayne, T. Leclerc, P. Sauer, R. Crabbs, and J. Kiriazes, "Near-ground vertical profile of refractive-index fluctuations," in *Atmospheric Propagation VI*, vol. 7324 (International Society for Optics and Photonics, 2009), p. 732402.
47. E. M. Dewan, *A Model for C_n^2 (Optical Turbulence) Profiles using Radiosonde Data*, 1121 (Directorate of Geophysics, Air Force Materiel Command, 1993).
48. R. Good, R. Beland, E. Murphy, J. Brown, and E. Dewan, "Atmospheric models of optical turbulence," in *Modeling of the Atmosphere*, vol. 928 (SPIE, 1988), pp. 165–186.
49. R. R. Beland, "Propagation through atmospheric optical turbulence," *Atmospheric Propag. Radiat.* **2**, 157–232 (1993).
50. S. Hagelin, E. Masciadri, and F. Lascaux, "Optical turbulence simulations at Mt Graham using the Meso-NH model," *Mon. Not. R. Astron. Soc.* **412**(4), 2695–2706 (2011).
51. E. Masciadri and S. Egner, "First seasonal study of optical turbulence with an atmospheric model," *Publ. Astron. Soc. Pac.* **118**(849), 1604–1619 (2006).
52. P. Bougeault, C. De Hui, B. Fleury, and J. Laurent, "Investigation of seeing by means of an atmospheric mesoscale numerical simulation," *Appl. Opt.* **34**(18), 3481–3488 (1995).
53. J. W. Deardorff, "Stratocumulus-capped mixed layers derived from a three-dimensional model," *Boundary-Layer Meteorol.* **18**(4), 495–527 (1980).
54. R. R. Beland and J. H. Brown, "A deterministic temperature model for stratospheric optical turbulence," *Phys. Scr.* **37**(3), 419–423 (1988).

55. F. H. Ruggiero and D. A. DeBenedictis, "Forecasting optical turbulence from mesoscale numerical weather prediction models," in *DoD High Performance Modernization Program Users Group Conference*, (2002), pp. 10–14.
56. F. Quatresooz, D. Vanhoenacker-Janvier, and C. Oestges, "Computation of optical refractive index structure parameter from its statistical definition using radiosonde data," *Radio Sci.* **58**(1), 1 (2023).
57. R. B. Stull, *An Introduction to Boundary Layer Meteorology*, vol. 13 (Springer Science & Business Media, 1988).
58. C. Ullwer, D. Sprung, E. Sucher, T. Kociok, P. Grossmann, A. M. van Eijk, and K. Stein, "Global simulations of Cn2 using the Weather Research and Forecast Model WRF and comparison to experimental results," in *Laser Communication and Propagation through the Atmosphere and Oceans VIII*, vol. 11133 (SPIE, 2019), pp. 126–136.
59. G. Jumper, "Thermosonde and radiosonde data from the T-REX campaign," (2006). Documentation from <https://data.eol.ucar.edu/dataset/92.048>.
60. G. Jumper, "T-REX: AFRL Radiosonde and Thermosonde Data," (2007). Version 1.0. UCAR/NCAR - Earth Observing Laboratory. <https://doi.org/10.26023/6HCG-E9WC-H0E>. Accessed 25 June 2021.
61. E. Masciadri, F. Lascaux, and L. Fini, "MOSE: operational forecast of the optical turbulence and atmospheric parameters at European Southern Observatory ground-based sites—I. Overview and vertical stratification of atmospheric parameters at 0–20 km," *Mon. Not. R. Astron. Soc.* **436**(3), 1968–1985 (2013).
62. F. Lascaux, E. Masciadri, and S. Hagelin, "Mesoscale optical turbulence simulations at Dome C: refinements," *Mon. Not. R. Astron. Soc.* **403**(4), 1714–1718 (2010).